Radar and ground-level measurements of clouds and precipitation collected during the POPE 2020 campaign at Princess Elisabeth Antarctica

Alfonso Ferrone[1, 2] and Alexis Berne[1]

[1]Environmental Remote Sensing Laboratory, École Polytechnique Fédérale de Lausanne (EPFL), Lausanne, Switzerland
[2]MeteoSwiss, via ai Monti 146, Locarno, Switzerland

Correspondence: Alexis Berne (alexis.berne@epfl.ch)

Abstract. The datasets presented in this article were collected during a four-months measurement campaign at the Belgian research base Princess Elisabeth Antarctica (PEA). The campaign, named PEA Orographic Precipitation Experiment (POPE), was conducted by the Environmental Remote Sensing Laboratory of the École Polytechnique Fédérale de Lausanne, with the logistical support of the International Polar Foundation, between the end of November 2019 and the beginning of February 2020. The datasets have been collected at five different sites. A W-band Doppler cloud profilers and a Multi-Angle Snowflake Camera (MASC) have been deployed in the immediate proximity of the main building of the station. An X-band dual-polarization Doppler scanning weather radar was installed 1.9 km south-east of PEA. Information on the various hydrometeor types have been derived from its measurements, as well as from the images collected by the MASC. The remaining three sites were located in a transect across the mountain chain south of the base, between 7 and 17 km apart from each other. At each site, a K-band Doppler profiler and an automated weather station have been deployed. A pyrgeometer and a pyranometer accompanied the instruments at the site in the middle of the transect. A case study, covering the precipitation event recorded on 23 December 2019, is presented to illustrate the various datasets. Overall, the availability of radar measurements over a complex terrain, relatively far from a scientific base, is extremely rare in the Antarctic context, and opens a wide range of possibilities for precipitation studies over the region.

1 Introduction

Princess Elisabeth Antarctica (PEA) is a polar research base owned by the Belgian government and managed by the International Polar Foundation (IPF). The station has been built on the Utsteinen nunatak in the immediate vicinity of the Sør Rondane Mountains, a mountain chain located in the Queen Maud Land region of East Antarctica. While the altitude of PEA is 1382 m above the mean sea level (a.m.s.l.), the tallest peaks in a 30 km radius from it reach up to up to 3000 m. With its distance of approximately 180 km from the coast, the base is also one of the few inland scientific facilities on the Antarctic continent. Its period of operation is limited to the sole austral summer, even though few permanent scientific observatories have been installed in its close vicinity and are able to collect measurements all-year round.

The surface mass balance (SMB)of the Queen Maud Land has been studied, as well as the influence of precipitation. In general, the importance of the latter lies in its role as the main input to the SMB of the Antarctic ice sheet (Van Wessem et al., 2018). Given the extension of the continent and the inner variability in meteorological and climate conditions, differences can be expected between the amount and frequency of precipitation in each location. In-situ measurements (Braaten, 2000; Fujita et al., 2011) and simulation results (Schlosser et al., 2010) suggest that in Queen Maud land few substantial events are the main contributors to the total snowfall accumulation. Given the aforementioned role of precipitation, these events are also the major contributors to the local SMB (Boening et al., 2012), and Medley et al. (2018) suggests that the recent increase in precipitation over the region may partially mitigate the the local loss of ice mass from the continent.

Focusing the analysis to PEA, local measurements confirm the relevance of these few significant events. The precipitation events themselves have been characterized by Gorodetskaya et al. (2013), identifying the strong easterly winds, high specific humidity, increased temperature, low atmospheric pressure, and the vicinity to a cyclonic system as the typical conditions under which they occur. A later study by Gorodetskaya et al. (2014) investigated the role of atmospheric rivers and their poleward transport of moisture, identifying this mechanism as the one responsible for the largest part of the accumulation at PEA between May 2009 and February 2011.

Measurements at PEA are not limited to the ground-level meteorological variables used in the two studies mentioned above. Since 2010, a Micro Rain Radar 2 (MRR-2), a profiling K-band (24 GHz) Doppler weather radar manufactured by Metek (Klugmann et al., 1996), has been installed on the rooftop of PEA, alongside a ceilometer and an upward-looking infrared pyrometer. This installation, as part of the HYDRANT observatory, is described by Gorodetskaya et al. (2015), who provides also an example of the possible applications of the collected datasets: the first characterization of clouds and precipitation at the site. A later study by Durán-Alarcón et al. (2019) used the same dataset to continue the characterization of snowfall at the site, focusing on the distinction between precipitation that sublimates before reaching the surface (virga) and the one that instead arrives at the ground.

The same radar measurements allowed a variety of scientific investigations on different topics. For instance, Souverijns et al. (2018b) used them to evaluated satellite-based radar products. A similar comparison, focusing on the snowfall rate, is presented by Lemonnier et al. (2019). The availability of the MRR-2 at the ground offers also an opportunity to focus on some limitations of satellite measurements, as shown by Maahn et al. (2014) in regard to the radar blind zone above the surface. Additional topics investigated thanks to the MRR-2 datasets collected at PEA include the study of the relationship between the radar reflectivity factor and the snowfall rate at the site (Souverijns et al., 2017), and the local contribution of precipitation to the surface mass balance (Souverijns et al., 2018a).

The relatively high number of studies that were enabled by the availability of this dataset underlines the importance of radar measurements in inland Antarctica. A major contribution to its importance is its multi-year time span, which makes it possible to capture changes even on the annual scale. However, the fixed location at which the instrument has been installed does not permit an analysis of the spatial variation in snowfall over the surroundings of the base. In an attempt to address this scientific questions, the Environmental Remote Sensing Laboratory of the École Polytechnique Fédérale de Lausanne (EPFL-LTE), with the logistical support of the IPF, designed and conducted a measurement campaign taking place at PEA and

in its vicinity. The project has been named PEA Orographic Precipitation Experiment (POPE), underlying the importance of monitoring snowfall over the complex terrain directly south of the base, and the resulting variability. The field campaign took place between 23 October 2019 and 11 February 2020, even though the period of data collection varies between the various scientific instruments that took part to the campaign. The instrument set includes remote-sensing ones, such as weather and cloud radars, and instruments providing information at the ground level, as Automated Weather Stations (AWS), a Multi-Angle Snowflake Camera (MASC) and radiometers. Part of this instrumentation has been deployed in a transect across the mountains directly south of PEA, reaching a maximum distance of 30 km from the base and representing one of the major novelties of this campaign.

This article presents the data collected during the POPE measurement campaign. Section 2 describes the sites, the scientific instruments deployed at each of them and the data they collected. Section 3 details the processing of the measurements. Section 4 presents a brief analysis of a precipitation event, illustrating some of the measurements and the derived quantities available in the datasets. Finally, Section 5 concludes the article.

2 Measurement sites and instruments

The characterization of the spatial variability of snowfall over the complex terrain surrounding PEA is the scientific question motivating the POPE campaign. To capture this spatial variability, instruments have been deployed at different sites. Their locations are illustrated in Figure 1 by a series of markers overlaid to the digital elevation model (Howat et al., 2019) of the region. Each of these sites and the associated measurements will be presented in order of distance from PEA.

2.1 Instruments at the base

Two scientific instruments have been installed in the immediate vicinity of PEA. This choice was mostly dictated by logistical constraints, related either to a high power consumption or the need for a frequent access to the measuring device.

The W-band Doppler cloud profiler and the Multi-Angle Snowflake Camera (MASC), were able to collect valid measurements for the majority of the deployment period. It should be mentioned that a tropospheric lidar and a weighing precipitation gauge were also deployed, but suffered from technical problems and unfortunately no valid data was recorded during the campaign. These two instruments will not be further discussed in the following.

2.1.1 W-band Doppler cloud profiler

A vertically-pointing W-band (94 GHz) Doppler cloud radar (Küchler et al., 2017), hereafter referred to as WProf, was deployed on a wooden pallet fixed to ice-free rocks of the ridge south of PEA. This radar, officially known by the commercial name of RPG-FMCW-94-SP, is developed by Radiometer Physics GmbH (RPG). This instrument has been collecting measurements between 27 November 2019 and 6 February 2020. However, the first days of deployment saw multiple changes in the configuration of the instrument and have been excluded from the dataset, whose initial date is therefore moved to 4 December

2019. A metal shipping container, used as shelter for the data acquisition systems by several scientific experiments, is present on the same ridge, approximately 10 meters to the north-east of the radar.

90   This instrument allows a large degree of flexibility when deciding the configuration used for the data acquisition. In our case, the final decision was a three-fold split of the chirp table, which divides the vertical extent into three consecutive sections. The parameters chosen for the period from 4 December 2019 onward are detailed in Table 1.

2.1.2   Multi-Angle Snowflake Camera

The MASC provides high-resolution pictures of ice hydrometeors falling through its detection area, as well as an estimate of
95   their vertical velocity. At its core are three cameras, laying on the same plane and pointing, with an angular separation of $36°$, towards a common focal point at about 10 cm distance from each of them. This focal point is in the middle of a metal ring, on which a system of infrared emitters at different heights triggers the cameras and provides the information needed for the fall speed computation (Garrett et al., 2012).

    The MASC was deployed on the rooftop of the central PEA building, at the coordinates -71.9499 N, 23.3471 E. The instru-
100   ment was installed on a metal pole, fixed to the railings of the base, in the immediate proximity of the permanent ceilometer installation, part of the HYDRANT observatory described by Gorodetskaya et al. (2013). The MASC was operational between 28 November 2019 and 05 February 2020, but a problem in the power supply resulted in a lack of measurements for the period from 10 to 17 January 2020. During its operational period, the instrument captured 17353 image triplets. The data collected by the MASC and some derived quantity, such as the classification of the hydrometeor types (Praz et al., 2017) and the detection
105   of blowing snow (Schaer et al., 2020), are accessible as part of the MASCDB library (Grazioli et al., 2022) and are therefore not been included in the dataset associated with the present article.

2.2   X-band dual-polarization Doppler scanning weather radar

The second site of the measurement campaign was approximately 1.9 km to the south-east of PEA, a few hundreds meter east of the Utsteinen Nunatak, as visible in Figure 1. At this location we deployed an X-band (9.41 GHz) scanning Doppler dual-
110   polarization weather radar (MXPol), equipped with a magnetron in its transmission chain, developed by Prosensing (Schneebeli et al., 2013).

    The scanning capabilities of this instrument allow the radar to monitor the surrounding area, collecting data along the direction in which the antenna moves. The types of scans performed during this campaign can be divided into two categories: Range-Height Indicator (RHI), during which the radar azimuth stays constant, while the elevation is changed, and Plan Position
115   Indicator (PPI), in which the elevation is kept fixed while the antenna rotates in azimuth. Typically, a series of PPI and RHI is repeated in a fixed order, defining the scanning cycle for the campaign, which was repeated indefinitely during operation.

    The radar has been collecting measurements discontinuously for the period between 16 December 2019 and 5 February 2020, being usually manually activated before precipitation events. The position of the radar has been chosen as a trade-off between ease of access, needed to operate it on a regular basis, and visibility on the mountain range. Since the only major
120   obstacle in its vicinity was the nunatak on the west, MXPol had a clear view on the base, most of the southern peaks and on

the North-East, direction of the typical flow associated with precipitation systems. These conditions on the visibility led us to define two different types of scan cycles.

The first of them was dedicated to the monitoring of widespread precipitation events, covering a large part of the area around the radar. It comprises:

125   – an RHI at 165.7° of azimuth, directed towards the location of the MRR-PRO 23;

    – an RHI at 190.1° of azimuth, conducted along an imaginary line passing in between the MRR-PRO 06 and MRR-PRO 22;

    – an RHI at 219.1° of azimuth, pointing towards the Vikinghogda, one of the main mountain peaks in the surroundings;

    – an RHI at 318.1° of azimuth, passing above PEA;

    – an RHI at 39.10° of azimuth, approximately along the NE and completing the hemispherical trajectory initiated by the
130   RHI scan at 219.1°;

    – a PPI at 4.4° of elevation, chosen to avoid excessive clutter contamination from the mountains;

    – a PPI at 88.9° of elevation, acting as nearly-vertical profile and providing measurements for the calibration of Z_{DR}.

The first three RHI scans have been performed in in Fast Fourier Transform (FFT) mode, and the elevation span has been limited between 0.9° and 68.9° to reduce the execution time. The remaining ones, instead, are performed in Dual-Pulse Pair
135 (DPP) mode and terminate at higher elevations, respectively equal to 88.9° and 108.9°. From the PPI scan at 4.4°, we excluded the azimuth sector between 244.4° and 314.7°, to remove the influence of the nunatak nearby.

The second cycle instead has been designed to monitor the small-scale precipitation events visible directly above some of the mountain peaks. In addition to the previously discussed RHI scans toward the MRR-PRO sites, the cycle includes:

    – an RHI at 134.0° of azimuth, pointing towards a mountain peak, close to the Verheyefjellet, over which isolated clouds
140   and precipitation were sometimes visible;

    – an RHI at 141.3° of azimuth, directed at another peak, with a similar location and set of characteristics as the previous one;

    – a sector scan (akin to a PPI, but limited in the azimuth extent) at 4.4° of elevation, covering between 127.1° and 234.8° of azimuth, providing visibility over most of the mountain range.

145 These scans have been performed in FFT mode. All the angles presented in the two cycles have been corrected for the azimuth and elevation offset of the antenna. The determination of the two biases is described in section 3.1.1. The different directions of the RHI scans are displayed as lines departing radially from the MXPol site in Figure 1, with color and style used to distinguish between the two cycles.

The decision between the DPP and FFT mode has a significant impact on the final products. Firstly, the full Doppler spectrum
150 is available only for the files generated by FFT scans, which will result in a slower antenna movement and larger file sizes. The

ones recorded in DPP mode, instead, create smaller files, and the scan instead is typically faster, which plays a role in deciding the composition of a cycle. The type of the scan also affects the Nyquist velocity: for the FFT ones it has been set to 11 m/s, for the DDP ones to 39 m/s.

155   With the sole exception of the PPI scan at 88.9° of elevation, measurements are collected up to a distance of 28.8 km from the radar for DPP scans, and of 27.6 km for the FFT ones, both with a range resolution of 75 m. The nearly-vertical PPI, instead, has been limited to a maximum range of 4.8 km, with a resolution of 30 m, to reduce the execution time while focusing solely on the lower region of the atmosphere, more likely to contain meteorological signal.

2.3   Transect of K-band Doppler profilers

Three Micro Rain Radars PRO (MRR-PRO), a model of K-band Doppler profilers manufactured by Metek, have been deployed
160 over a transect across the mountains directly south of PEA. Their small size and low power consumption made them the perfect fit for deployment in remote sites, with limited access to maintenance and no connection to the power grid of PEA.

    The transect comprises the three different locations shown in Figure 1, approximately between 7 and 17 km apart from each other, and a maximum distance from PEA of 30 km. To distinguish the three sites we will use the serial number of the radar deployed in each of them:

165   – MRR-PRO 06, deployed close to one of the mountain ridges (latitude -72.118, longitude 23.347). Its position has been chosen as a compromise between the need of getting as close as possible to the mountain peaks and the accessibility constraints of the region. The chosen location is at an altitude of 2000 m a.m.s.l.

      – MRR-PRO 22, deployed at the beginning of the plateau (latitude -72.227, longitude 23.191). This location is the highest of the three (2360 m a.m.s.l.). Given its position relative to the nearby orography, it can also be generally considered
170   downstream of the mountain top in the typical atmospheric flow during significant precipitation events.

      – MRR-PRO 23, deployed in a valley connecting the plateau to the lower plains (latitude -72.114, longitude 23.514). This is the lowest of the three locations (1543 m a.m.s.l.), just about 150 m above PEA (1382 m a.m.s.l.). It is also East of the main peaks, implying an upstream position with respect to the mountain.

    The precise choice of the three locations is further explained in Appendix A. The duration of each collection period varies
175 slightly among the three profilers: 11 December 2019 to 27 January 2020 for the MRR-PRO 06, 14 December 2019 to 28 January 2020 for the MRR-PRO 22, 12 December 2019 to 28 January 2020 for the MRR-PRO 23.

2.3.1   Automated weather stations and radiometers

An automated weather station, manufactured by Vaisala (models WXT536 and WXT520), has been installed in the vicinity of each of the MRR-PRO, at an height of approximately 1.5 m above the ground. The values of wind direction and speed,
180 atmospheric pressure, air temperature, and relative humidity with respect to liquid water have been collected ensuring time synchronization with the radar measurements.

Additionally, a pyranometer (manufactured by Kipp & Zonen, model CMP3) and a pyrgeometer (Kipp & Zonen, CGR3) have been deployed alongisde the MRR-PRO 06, on an horizontal pipe connecting the radar to the AWS. The two radiometers provide estimates of the total downwelling irradiance, respectively in the shortwave (wavelength range between 300 nm and 2800 nm) and the longwave (4500 nm to 42000 nm).

185

3 Data processing

This section focuses on the meteorological radars, describing the procedure followed in deriving the radar variables from the raw data and the calibration techniques used to ensure the accuracy of the measurements. The processing of measurements collected by the AWS and radiometers is limited to the removal of non-numerical characters from the time-series and the storage in netCDF4 format (Unidata, 2019), and therefore has not been discussed further in this section.

190

3.1 MXPol

The processing of the data collected by MXPol follows closely the steps described by Gehring et al. (2021) for the same radar during the ICE-POP 2018 campaign in South-Korea. Starting from the raw spectra collected by the instrument, the method of Hildebrand and Sekhon (1974) is used for isolating the signal from the noise floor. The former contains the information needed to determine the polarimetric variables, according to the backscatter covariance matrix procedure illustrated by Doviak and Zrnic (1993). The creation of the data files is performed using the Python library PyART (Helmus and Collis, 2016).

195

The processing produces the following radar variables:

- Z_H and Z_V, the horizontal and vertical reflectivity factors, stored in logarithmic form and having the units dBZ;

- Z_{DR}, the differential reflectivity, also stored in logarithmic form and expressed in dB;

200

- SNR_H and SNR_v, the signal-to-noise ratio on the two polarization channels, in dB;

- V, the mean Doppler radial velocity, whose units are ms^{-1};

- SW, the spectral width, also expressed in ms^{-1};

- Φ_{DP}, the total differential phase shift, in degrees;

- K_{DP}, specific differential phase on propagation, in $^\circ\,\mathrm{km}^{-1}$, estimated using the method described by Schneebeli et al. (2014);

205

- ρ_{hv}, the co-polar correlation coefficient, dimensionless.

3.1.1 Correction of the azimuth and elevation offset

Since MXPol is a scanning weather radar, each of its measurements is characterized by an azimuth and elevation angle. The complexity of the deployment on an ice surface, in a rather remote site, makes achieving a perfect alignment of the antenna

210 extremely difficult. Therefore, an offset that compensates for any misalignment must be computed and subtracted from the angle recorded by the radar.

On the 07, 08, 10 and 13 January we performed a series of scans covering a small windows of azimuth and elevation angles around the position of the Sun. By comparing the apparent position of the center of the Sun as seen by the radar with its expected position provided by the Python library Astropy (Astropy Collaboration et al., 2018), we can estimate the offset.

215 This approach is loosely based on the method described by Muth et al. (2012). Our estimate of the offsets are: $108.11°$ for the azimuth, $1.05°$ for the elevation.

The validity of the azimuth estimate has been controlled by pointing the antenna towards recognizable mountain peaks on the south of PEA, checking the difference between the angle of each geographical feature with the one recorded by the radar. The average difference recorded among the five targets tested is $0.2°$, within the expected accuracy for a manual pointing.

220 ### 3.1.2 Calibration

The radar underwent a control of the stability of the signal in July 2018, during a short deployment in Remoray (France). The calibration was performed by Palindrome Remote Sensing GmbH, using a radar target simulator (Schneebeli and Leuenberger). Overall, the information collected during this short deployment show that the reflectivity factor recorded by MXPol is within $1\,\mathrm{dBZ}$ of the real value.

225 ### 3.1.3 Correction of the differential reflectivity bias

Depending on the target and application, the differential reflectivity measurements require to be calibrated with an accuracy that varies between $0.1\,\mathrm{dB}$ and $0.2\,\mathrm{dB}$ (Ryzhkov et al., 2005). To ensure that our measurements satisfy this condition we computed a time-varying offset using the method described by Ferrone and Berne (2021). According to this technique, the offset values are derived from the vertical PPI scans performed by the radar at regular intervals. Their time variability is determined by a fit

230 of the semi-variogram, whose parameters are used for a 1-dimensional ordinary kriging interpolation of the offset of each scan. For this measurement campaign, we used a spherical model for the fit with the following parameters: the nugget is $0.0021\,\mathrm{dB}^2$, the range is $540\,\mathrm{min}$ and the sill is $0.0043\,\mathrm{dB}^2$. The final interpolation output is shown in Figure 2, superimposed to the offset computed from each PPI scans.

3.1.4 Determination of the hydrometeor types

235 The polarimetric variables collected during the RHI scans performed by MXPol have been used to identify the dominant hydrometeor type, according to the algorithm of Besic et al. (2016). The centroids used in the procedure are the same ones mentioned by Gehring et al. (2021), computed on past datasets collected by the same radar. The same scans have been used to determine the hydrometeor mixture in the radar volumes, using the method described by Besic et al. (2018).

3.2 WProf

240 Differently to the MXPol case, the raw spectra collected by WProf were not saved in their entirety. Only the power identified by the radar as signal, according to the radar own algorithm (Küchler et al., 2017), has been preserved. From this signal, the following radar variables have been computed: equivalent reflectivity factor (Z, expressed in the linear units $\mathrm{mm}^6\mathrm{m}^{-3}$), signal to noise ratio (SNR, in dB), V, SW, skewness, and kurtosis (in ms^{-1}). Additionally, WProf includes an 89 GHz radiometer, which allowed the retrieval of the liquid water path and integrated water vapor unsing the algorithm described by Billault-Roux
245 and Berne (2021).

3.2.1 Correction of the attenuation by atmospheric gasses

The attenuation of atmospheric gasses has been computed following a procedure analogous to the one used by Gehring et al. (2021) for the same radar, recommended also by Ippolito (1986). The profiles of atmospheric pressure, air temperature and humidity recorded by the radiosoungins performed from one of the secondary facilities of the base, at few hundred meters from
250 the deployment site of WProf, have been used as input for the algorithm. However, given the low values of attenuation, below than 0.1 dB, we decided not to add the correction to the files in the dataset.

3.3 MRR-PRO

The internal algorithm of the MRR-PRO designed by Metek for the computation of the radar variables is targeted mostly toward observations of liquid precipitation. Moreover, the measurements are sometimes affected by artefacts that cover a small subset
255 of the range gates and can hinder the correct interpretation of the meteorological signal. Other issues in the measurements include a drop in the power recorded in the raw Doppler spectra in the lines adjacent the extremes of the Nyquist velocity interval. To address these issues, the MRR-PRO data have been processed by the ERUO library (Ferrone et al., 2022), which acts on the raw Doppler spectra to extract a cleaner set of radar variables. ERUO also performs a simple dealiasing in the Doppler velocity measurements, and increases the sensitivity in the profiles of attenuated equivalent reflectivity factor. The
260 final set of variables computed for the three MRR-PRO is analogous to the WProf one, with the exception of skewness and kurtosis, which have not been included in the dataset, but can still be derived from the Doppler spectra and noise level available in the data files.

3.4 Sensitivity of the radars

In Figure 3, we illustrate the 2-dimensional distribution of the attenuated equivalent reflectivity factors recorded by WProf
265 and during the vertical PPI scans of MXPol. A threshold of 0 dB has been imposed on the signal-to-noise ratio of the two radars, in order to exclude faint non-meteorological returns from the comparison. The left side of the distributions of the WProf reflectivity factor reaches consistently lower values when compared with MXPol, indicating that the former has a higher sensitivity than the latter.

Earth System
Science
Data

Discussions

Open Access

270   In panel 3.a, clusters of high counts can be observed at range values between 1 and 1.5 km. This behavior is caused by artefacts in the radar data that, unlike the MRR-PRO case, could not be filtered out during processing. The artefacts are usually covered by relatively strong precipitation signal (above 10 dBZ), but visible when the meteorological return is faint. While this behavior would significantly limit the usefulness of the dataset for a profiler, the scanning capability of MXPol and the large visibility radius results in a majority of the radar volumes being unaffected during RHI and low-elevation PPI scans.

Panel 3.b illustrates a particularity of the measurement configuration of WProf. Sudden variations can be observed in the
275   minimum of the distributions at the transition between the chirps defined in Table 1.

The sensitivity curves of the three MRR-RPO have not been included in the current article, since they are already shown and discussed by Ferrone et al. (2022). By comparing the three datasets, a significant difference between the MRR-PRO 22 curve and the ones from the other two MRR-PRO can be noticed. We hypothesize that this difference is caused by miscalibration issues, but we could not directly test the agreement between the three profilers before or after their deployment at PEA.

280   The difference between the quantile 0.01 of the MRR-PRO 06 distributions and the MRR-PRO 22 one is 9 dB, while the one between MRR-PRO 23 and MRR-PRO 22 is 11 dB. For both sets of differences, the interquartile range is 2 dB. Therefore, a value of 10 dB should be added to the equivalent attenuated reflectivity factor measured by the MRR-PRO 22 before comparing it to the other two profilers in the transect. However, due to the approximate nature of this offset, and the impossibility of comparing the MRR-PRO 22 with an adequate reference set of measures, we decided not to add the 10 dB to
285   the MRR-PRO measurements provided in the publicly accessible datasets.

4   Significant weather events

Since the weighing precipitation gauge was not able to record valid measurements during the campaign, it cannot be used as reference for identifying the start and end date of snowfall events at the base. For this reason, we have decided to use the time-series provided by the three MRR-PRO to identify the frequency of precipitation in our datasets, identifying 10 separated
290   events in which most of the instruments have collected valid measurements. The detection rate varies between radars, due to their different sensitivity. For instance, WProf is able to detect the faint return of clouds, resulting in a higher number of days in which meteorological signal is observed. In the following subsection, the precipitation event recorded on the 23 December 2019 is presented to illustrate the variety of products in the datasets described in the present article.

4.1   23 December 2019

295   On 23 December 2019, significant precipitation has been observed by all instruments part to the POPE campaign. Figure 4 shows the time series of reflectivity factor from WProf, MXPol, and the three MRR-PRO

Thanks to its high sensitivity, WProf provides a clear view of the vertical structure of precipitation above the base, detecting meteorological signal up to 7 km above the surface. Similar features can be observed in the time-series recorded by MXPol, even though the vertical extent is significantly lower. As mentioned in section 3.4, artefacts are visible in the data, appearing
300   as horizontal lines in the range gates between 1 and 1.5 km.

Over the transect, MRR-PRO 06 and MRR-PRO 22 record meteorological signal more continuously than MRR-PRO 23. In the highest of the three locations, precipitation reaches the lowest range gate more often than for the other two profilers. In particular, virga are present in the MRR-PRO 23 time-series in the early and late stages of the event.

The complementary measurements provided by the three AWS and the radiometers are shown in Figure 5. The difference in
305   air temperature between the sites in the transect is consistent with their elevation difference. The relative humidity values experience more significant fluctuations, especially at the MRR-PRO 23 site. In particular, high humidity values can be observed for some periods at the beginning and end of the event, following a pattern similar to the aforementioned virga. A similar difference in behavior between sites can be seen also for the wind direction. The north-eastern direction is dominant in the MRR-PRO 06 and MRR-PRO 22 time series. The location of the MRR-PRO 23 within a valley could explain the difference
310   from the other two sites, with sudden oscillation between a northerly and southerly flow approximately aligned to the valley orientation. The relatively low values of shortwave irradiance at the MRR-PRO 06, visible in panel 5.e, confirm the presence of clouds for most of the day.

Information on the hydrometeor types can be derived from both the MASC and the RHI scans performed by MXPol. Figure 6 shows such information for the event currently described. Given the variety of scans in the two cycles, we decided to limit the
315   analysis to the sole RHI directed toward the base. The proportion of three hydrometeor types (crystals, aggregates and rimed particles) has been computed using the algorithm designed by Besic et al. (2018). In order to display the values in an easily readable time-series, these proportions have been averaged over the radar volumes with an horizontal distance lower than 500 m from the base, obtaining a mean profile for each scan. A vertical resolution of 75 m has been used to create the profiles.

Crystals dominate the whole time series, followed by aggregates, especially in the lowest section of the profile. Rimed
320   particle are less frequent, reaching maximum values barely above 10 %, mostly close to the ground level. While MXPol records precipitation during the whole day, the MASC experiences extended period of lack of observations. Small particles are particularly abundant, even though blowing snow has been filtered out from the dataset. Graupel is also relatively common, despite the lack of rimed particles in the MXPol data. Aggregates appear more often during the first phase of the event, with crystals overtaking them in proportion after 06:00 UTC.

325   # 5   Conclusions

This article presents datasets collected by meteorological radars and ground-level instruments between November 2019 and February 2020 in the surroundings of the Belgian research base Princess Elisabeth Antarctica. The scientific equipment has been deployed and maintained by the EPFL-LTE laboratory, with the logistical support of IPF, in the context of the PEA Orographic Precipitation Experiment (POPE). This project has among its main objectives the characterization of snowfall over
330   the complex terrain around PEA.

The main novelty of POPE is the deployment of three K-band Doppler profilers (MRR-PRO) and automated weather station in a transect across the mountain range, reaching a distance of 30 km from the base. A pyranometer and a pyrgeometer

accompany one of the profilers in the transect. An X-band Doppler dual-polarization scanning radar, a W-band Doppler cloud profiler and a multi-angle snowflake camera have been installed in the vicinity of PEA.

335　　The availability of polarimetric and Doppler radar measurements, accompanied by snowflake pictures collected at the base, make this dataset particularly suited for snowfall microphysics studies. Additionally, the variety in the locations allows investigation on the spatial variability of snowfall. Future studies may use the datasets presented in this article to improve the current understanding of precipitation in this region of the Antarctic continent.

6　Data availability

340　　The datasets described in this article are available at: https://doi.org/10.5281/zenodo.7006309 (Ferrone and Berne, 2022). Given the large size of the Doppler spectra collected by WProf and MXPol, we decided to exclude them from the online repository. While the radar moments and the derived quantities can be directly accessed from the link above, the Doppler spectra can instead be requested from the corresponding author.

Appendix A:　Choice of the MRR-PRO locations based on the output of atmospheric simulations

345　　To determine the exact locations of the three sites, we used the output of a series of atmospheric simulations, made by using the version 4.0 of the Weather Research and Forecasting (WRF) model (Skamarock et al., 2021) and covering the three Austral summers preceding the campaign, from December 2014 to February 2107. The parent domain has a resolution of 27 km and it contains three nested domains, of 9 km, 3 km and 1 km resolution, centered around PEA. This elevation has been derived from the Bedmap2 1-km resolution Antarctic topography (Fretwell et al., 2013), and the model has been run with 69 vertical levels.

350　　The ERA5 reanalysis has been used to define the boundary and initial conditions. Additional information on the nudging of the parent domain and the physical parameters can be found in Vignon et al. (2019), which describes a set-up akin to the one used for the current analysis.

　　In all three simulations, a local maximum of precipitation can be found on the mountain chain directly south of PEA, while the valley that connects the plateau to the lower elevations is usually characterized by smaller accumulations. Repeating the

355　simulations for the period December 2019 to January 2020 shows a similar pattern, illustrated in Figure A1.

　　While the final decision on the precise locations of the MRR-PRO sites is mostly determined by logistical constraints given by the limited accessibility of remote areas, we attempted to capture the variability of the accumulation field around the aforementioned mountain group and nearby valley. As can be seen in Figure A1, the MRR-PRO 23 has been deployed in a location that receives significantly less precipitation at the ground when compared with the other two sites in the transect. The

360　MRR-PRO 06 is close to the mountain peak, and at the edge of the local accumulation maximum. The MRR-PRO 22 is also close to this maximum, but on the other side of the orography and, in the north-easterly flow typical of precipitation events in the region, can be considered downstream to the mountain.

Earth System
Science
Data

Open Access

Discussions

References

375 Astropy Collaboration, Price-Whelan, A. M., Sipőcz, B. M., Günther, H. M., Lim, P. L., Crawford, S. M., Conseil, S., Shupe, D. L., Craig, M. W., Dencheva, N., Ginsburg, A., Vand erPlas, J. T., Bradley, L. D., Pérez-Suárez, D., de Val-Borro, M., Aldcroft, T. L., Cruz, K. L., Robitaille, T. P., Tollerud, E. J., Ardelean, C., Babej, T., Bach, Y. P., Bachetti, M., Bakanov, A. V., Bamford, S. P., Barentsen, G., Barmby, P., Baumbach, A., Berry, K. L., Biscani, F., Boquien, M., Bostroem, K. A., Bouma, L. G., Brammer, G. B., Bray, E. M., Breytenbach, H., Buddelmeijer, H., Burke, D. J., Calderone, G., Cano Rodríguez, J. L., Cara, M., Cardoso, J. V. M., Cheedella, S., Copin, Y., Corrales, L.,

380 Crichton, D., D'Avella, D., Deil, C., Depagne, É., Dietrich, J. P., Donath, A., Droettboom, M., Earl, N., Erben, T., Fabbro, S., Ferreira, L. A., Finethy, T., Fox, R. T., Garrison, L. H., Gibbons, S. L. J., Goldstein, D. A., Gommers, R., Greco, J. P., Greenfield, P., Groener, A. M., Grollier, F., Hagen, A., Hirst, P., Homeier, D., Horton, A. J., Hosseinzadeh, G., Hu, L., Hunkeler, J. S., Ivezić, Ž., Jain, A., Jenness, T., Kanarek, G., Kendrew, S., Kern, N. S., Kerzendorf, W. E., Khvalko, A., King, J., Kirkby, D., Kulkarni, A. M., Kumar, A., Lee, A., Lenz, D., Littlefair, S. P., Ma, Z., Macleod, D. M., Mastropietro, M., McCully, C., Montagnac, S., Morris, B. M., Mueller, M., Mumford,

385 S. J., Muna, D., Murphy, N. A., Nelson, S., Nguyen, G. H., Ninan, J. P., Nöthe, M., Ogaz, S., Oh, S., Parejko, J. K., Parley, N., Pascual, S., Patil, R., Patil, A. A., Plunkett, A. L., Prochaska, J. X., Rastogi, T., Reddy Janga, V., Sabater, J., Sakurikar, P., Seifert, M., Sherbert, L. E., Sherwood-Taylor, H., Shih, A. Y., Sick, J., Silbiger, M. T., Singanamalla, S., Singer, L. P., Sladen, P. H., Sooley, K. A., Sornarajah, S., Streicher, O., Teuben, P., Thomas, S. W., Tremblay, G. R., Turner, J. E. H., Terrón, V., van Kerkwijk, M. H., de la Vega, A., Watkins, L. L., Weaver, B. A., Whitmore, J. B., Woillez, J., Zabalza, V., and Astropy Contributors: The Astropy Project: Building an Open-science

390 Project and Status of the v2.0 Core Package, The Astronomical Journal, 156, 123, https://doi.org/10.3847/1538-3881/aabc4f, 2018.

Besic, N., Figueras i Venturra, J., Grazioli, J., Gabella, M., Germann, U., and Berne, A.: Hydrometeor classification through statistical clustering of polarimetric radar measurements: a semi-supervised approach, Atmospheric Measurement Techniques, 9, 4425–4445, https://doi.org/10.5194/amt-9-4425-2016, 2016.

Besic, N., Gehring, J., Praz, C., Figueras i Ventura, J., Grazioli, J., Gabella, M., Germann, U., and Berne, A.: Unraveling hydrometeor

395 mixtures in polarimetric radar measurements, Atmospheric Measurement Techniques, 11, 4847–4866, https://doi.org/10.5194/amt-11-4847-2018, 2018.

Billault-Roux, A.-C. and Berne, A.: Integrated water vapor and liquid water path retrieval using a single-channel radiometer, Atmospheric Measurement Techniques, 14, 2749–2769, https://doi.org/10.5194/amt-14-2749-2021, 2021.

Boening, C., Lebsock, M., Landerer, F., and Stephens, G.: Snowfall-driven mass change on the East Antarctic ice sheet, Geophysical Research

400 Letters, 39, https://doi.org/https://doi.org/10.1029/2012GL053316, 2012.

Braaten, D. A.: Direct measurements of episodic snow accumulation on the Antarctic polar plateau, Journal of Geophysical Research: Atmospheres, 105, 10 119–10 128, https://doi.org/https://doi.org/10.1029/2000JD900099, 2000.

Doviak, R. and Zrnic, D. S.: Doppler radar and weather observations, Academic Press, Academic Press, San Diego, 1993.

Durán-Alarcón, C., Boudevillain, B., Genthon, C., Grazioli, J., Souverijns, N., van Lipzig, N. P. M., Gorodetskaya, I. V., and Berne, A.:

405 The vertical structure of precipitation at two stations in East Antarctica derived from micro rain radars, The Cryosphere, 13, 247–264, https://doi.org/10.5194/tc-13-247-2019, 2019.

Ferrone, A. and Berne, A.: Dynamic Differential Reflectivity Calibration Using Vertical Profiles in Rain and Snow, Remote Sensing, 13, https://doi.org/10.3390/rs13010008, 2021.

Ferrone, A. and Berne, A.: Radar and ground-level measurements collected during the POPE 2020 campaign at Princess Elisabeth Antarctica,

410 https://doi.org/10.5281/zenodo.7006309, 2022.

Open Access

Earth System
Science
Data

Discussions

Ferrone, A., Billault-Roux, A.-C., and Berne, A.: ERUO: a spectral processing routine for the Micro Rain Radar PRO (MRR-PRO), Atmospheric Measurement Techniques, 15, 3569–3592, https://doi.org/10.5194/amt-15-3569-2022, 2022.

Fretwell, P., Pritchard, H. D., Vaughan, D. G., Bamber, J. L., Barrand, N. E., Bell, R., Bianchi, C., Bingham, R. G., Blankenship, D. D.,
Casassa, G., Catania, G., Callens, D., Conway, H., Cook, A. J., Corr, H. F. J., Damaske, D., Damm, V., Ferraccioli, F., Forsberg, R., Fujita,
415   S., Gim, Y., Gogineni, P., Griggs, J. A., Hindmarsh, R. C. A., Holmlund, P., Holt, J. W., Jacobel, R. W., Jenkins, A., Jokat, W., Jordan,
T., King, E. C., Kohler, J., Krabill, W., Riger-Kusk, M., Langley, K. A., Leitchenkov, G., Leuschen, C., Luyendyk, B. P., Matsuoka, K.,
Mouginot, J., Nitsche, F. O., Nogi, Y., Nost, O. A., Popov, S. V., Rignot, E., Rippin, D. M., Rivera, A., Roberts, J., Ross, N., Siegert, M. J.,
Smith, A. M., Steinhage, D., Studinger, M., Sun, B., Tinto, B. K., Welch, B. C., Wilson, D., Young, D. A., Xiangbin, C., and Zirizzotti,
A.: Bedmap2: improved ice bed, surface and thickness datasets for Antarctica, The Cryosphere, 7, 375–393, https://doi.org/10.5194/tc-7-
420   375-2013, 2013.

Fujita, S., Holmlund, P., Andersson, I., Brown, I., Enomoto, H., Fujii, Y., Fujita, K., Fukui, K., Furukawa, T., Hansson, M., Hara, K., Hoshina,
Y., Igarashi, M., Iizuka, Y., Imura, S., Ingvander, S., Karlin, T., Motoyama, H., Nakazawa, F., Oerter, H., Sjöberg, L. E., Sugiyama, S.,
Surdyk, S., Ström, J., Uemura, R., and Wilhelms, F.: Spatial and temporal variability of snow accumulation rate on the East Antarctic ice
divide between Dome Fuji and EPICA DML, The Cryosphere, 5, 1057–1081, https://doi.org/10.5194/tc-5-1057-2011, 2011.

425   Garrett, T. J., Bair, E. H., Fallgatter, C. J., Shkurko, K., Davis, R. E., and Howlett, D.: The Multi-Angle Snowflake Camera, Proceedings,
2012 International Snow Science Workshop, Anchorage, Alaska, pp. 930–933, http://arc.lib.montana.edu/snow-science/item/1672, 2012.

Gehring, J., Ferrone, A., Billault-Roux, A.-C., Besic, N., Ahn, K. D., Lee, G., and Berne, A.: Radar and ground-level measurements of precipitation collected by the École Polytechnique Fédérale de Lausanne during the International Collaborative Experiments for PyeongChang
2018 Olympic and Paralympic winter games, Earth System Science Data, 13, 417–433, https://doi.org/10.5194/essd-13-417-2021, 2021.

430   Gorodetskaya, I. V., Van Lipzig, N. P. M., Van den Broeke, M. R., Mangold, A., Boot, W., and Reijmer, C. H.: Meteorological regimes and
accumulation patterns at Utsteinen, Dronning Maud Land, East Antarctica: Analysis of two contrasting years, Journal of Geophysical
Research: Atmospheres, 118, 1700–1715, https://doi.org/https://doi.org/10.1002/jgrd.50177, 2013.

Gorodetskaya, I. V., Tsukernik, M., Claes, K., Ralph, M. F., Neff, W. D., and Van Lipzig, N. P. M.: The role of
atmospheric rivers in anomalous snow accumulation in East Antarctica, Geophysical Research Letters, 41, 6199–6206,
435   https://doi.org/https://doi.org/10.1002/2014GL060881, 2014.

Gorodetskaya, I. V., Kneifel, S., Maahn, M., Van Tricht, K., Thiery, W., Schween, J. H., Mangold, A., Crewell, S., and Van Lipzig, N.
P. M.: Cloud and precipitation properties from ground-based remote-sensing instruments in East Antarctica, The Cryosphere, 9, 285–304,
https://doi.org/10.5194/tc-9-285-2015, 2015.

Grazioli, J., Ghiggi, G., Billault-Roux, A.-C., and Berne, A.: MASCDB, a database of images, descriptors and microphysical properties of
440   individual snowflakes in free fall, Scientific Data, 9, 186, https://doi.org/10.1038/s41597-022-01269-7, 2022.

Helmus, J. J. and Collis, S. M.: The Python ARM Radar Toolkit (Py-ART), a library for working with weather radar data in the Python
programming language, Journal of Open Research Software, 4, e25, https://doi.org/10.5334/jors.119, 2016.

Hildebrand, P. H. and Sekhon, R.: Objective determination of the noise level in Doppler spectra, Journal of Applied Meteorology, 13, 808–
811, https://doi.org/https://doi.org/10.1175/1520-0450(1974)013<0808:ODOTNL>2.0.CO;2, 1974.

445   Howat, I. M., Porter, C., Smith, B. E., Noh, M.-J., and Morin, P.: The Reference Elevation Model of Antarctica, The Cryosphere, 13, 665–674,
https://doi.org/10.5194/tc-13-665-2019, 2019.

Ippolito, L. J.: Attenuation by Atmospheric Gases, pp. 25–37, Springer Netherlands, Dordrecht, https://doi.org/10.1007/978-94-011-7027-
7_3, 1986.

Klugmann, D., Heinsohn, K., and Kirtzel, H. J.: A low cost 24 GHz FM-CW Doppler radar rain profiler, Contributions to Atmospheric
450   Physics, 69, 1996.

Küchler, N., Kneifel, S., Löhnert, U., Kollias, P., Czekala, H., and Rose, T.: A W-band radar–radiometer system for accurate and continuous
       monitoring of clouds and precipitation, Journal of Atmospheric and Oceanic Technology, 34, 2375–2392, 2017.

Lemonnier, F., Madeleine, J.-B., Claud, C., Genthon, C., Durán-Alarcón, C., Palerme, C., Berne, A., Souverijns, N., van Lipzig, N., Gorodet-
       skaya, I. V., L'Ecuyer, T., and Wood, N.: Evaluation of CloudSat snowfall rate profiles by a comparison with in situ micro-rain radar
455   observations in East Antarctica, The Cryosphere, 13, 943–954, https://doi.org/10.5194/tc-13-943-2019, 2019.

Maahn, M., Burgard, C., Crewell, S., Gorodetskaya, I. V., Kneifel, S., Lhermitte, S., Van Tricht, K., and van Lipzig, N. P. M.: How does the
       spaceborne radar blind zone affect derived surface snowfall statistics in polar regions?, Journal of Geophysical Research: Atmospheres,
       119, 13,604–13,620, https://doi.org/https://doi.org/10.1002/2014JD022079, 2014.

Medley, B., McConnell, J. R., Neumann, T. A., Reijmer, C. H., Chellman, N., Sigl, M., and Kipfstuhl, S.: Temperature and Snow-
460   fall in Western Queen Maud Land Increasing Faster Than Climate Model Projections, Geophysical Research Letters, 45, 1472–1480,
       https://doi.org/https://doi.org/10.1002/2017GL075992, 2018.

Muth, X., Schneebeli, M., and Berne, A.: A sun-tracking method to improve the pointing accuracy of weather radar, Atmospheric Measure-
       ment Techniques, 5, 547–555, https://doi.org/10.5194/amt-5-547-2012, 2012.

Praz, C., Roulet, Y.-A., and Berne, A.: Solid hydrometeor classification and riming degree estimation from pictures collected with a Multi-
465   Angle Snowflake Camera, Atmos. Meas. Tech., p. 23, 2017.

Ryzhkov, A. V., Giangrande, S. E., Melnikov, V. M., and Schuur, T. J.: Calibration Issues of Dual-Polarization Radar Measurements, J.
       Atmos. Oceanic Technol., 22, 1138–1155, https://doi.org/10.1175/JTECH1772.1, 2005.

Schaer, M., Praz, C., and Berne, A.: Identification of blowing snow particles in images from a Multi-Angle Snowflake Camera, The
       Cryosphere, 14, 367–384, https://doi.org/10.5194/tc-14-367-2020, 2020.

470   Schlosser, E., Manning, K. W., Powers, J. G., Duda, M. G., Birnbaum, G., and Fujita, K.: Characteristics of high-precipitation events in Dron-
       ning Maud Land, Antarctica, Journal of Geophysical Research: Atmospheres, 115, https://doi.org/https://doi.org/10.1029/2009JD013410,
       2010.

Schneebeli, M. and Leuenberger, A.: Radar Target Simulator, https://www.palindrome-rs.ch/products/radar-target-simulator/.

Schneebeli, M., Dawes, N., Lehning, M., and Berne, A.: High-resolution vertical profiles of X-band polarimetric radar observables during
475   snowfall in the Swiss Alps, Journal of applied meteorology and climatology, 52, 378–394, 2013.

Schneebeli, M., Grazioli, J., and Berne, A.: Improved Estimation of the Specific Differential Phase Shift Using a Compilation of Kalman
       Filter Ensembles, IEEE Transactions on Geoscience and Remote Sensing, 52, 5137–5149, https://doi.org/10.1109/TGRS.2013.2287017,
       2014.

Skamarock, W. C., Klemp, J. B., Dudhia, J., Gill, D. O., Liu, Z., Berner, J., Wang, W., Powers, J. G., Duda, M. G., Barker, D., and Huang,
480   X.-y.: A Description of the Advanced Research WRF Model Version 4.3, Tech. rep., NCAR Tech. Note, https://doi.org/doi:10.5065/1dfh-
       6p97, 2021.

Souverijns, N., Gossart, A., Lhermitte, S., Gorodetskaya, I., Kneifel, S., Maahn, M., Bliven, F., and van Lipzig, N.: Estimating radar reflec-
       tivity - Snowfall rate relationships and their uncertainties over Antarctica by combining disdrometer and radar observations, Atmospheric
       Research, 196, 211–223, https://doi.org/https://doi.org/10.1016/j.atmosres.2017.06.001, 2017.

485   Souverijns, N., Gossart, A., Gorodetskaya, I. V., Lhermitte, S., Mangold, A., Laffineur, Q., Delcloo, A., and van Lipzig, N. P. M.: How does
         the ice sheet surface mass balance relate to snowfall? Insights from a ground-based precipitation radar in East Antarctica, The Cryosphere,
         12, 1987–2003, https://doi.org/10.5194/tc-12-1987-2018, 2018a.

       Souverijns, N., Gossart, A., Lhermitte, S., Gorodetskaya, I. V., Grazioli, J., Berne, A., Duran-Alarcon, C., Boudevillain, B., Genthon, C.,
         Scarchilli, C., and van Lipzig, N. P. M.: Evaluation of the CloudSat surface snowfall product over Antarctica using ground-based precipi-
490   tation radars, The Cryosphere, 12, 3775–3789, https://doi.org/10.5194/tc-12-3775-2018, 2018b.

       Unidata: Network Common Data Form (NetCDF), https://doi.org/10.5065/D6H70CW6, 2019.

       Van Wessem, J. M., van de Berg, W. J., Noël, B. P. Y., van Meijgaard, E., Amory, C., Birnbaum, G., Jakobs, C. L., Krüger, K., Lenaerts, J.
         T. M., Lhermitte, S., Ligtenberg, S. R. M., Medley, B., Reijmer, C. H., van Tricht, K., Trusel, L. D., van Ulft, L. H., Wouters, B., Wuite,
         J., and van den Broeke, M. R.: Modelling the climate and surface mass balance of polar ice sheets using RACMO2 – Part 2: Antarctica
495   (1979–2016), The Cryosphere, 12, 1479–1498, https://doi.org/10.5194/tc-12-1479-2018, 2018.

       Vignon, E., Besic, N., Jullien, N., Gehring, J., and Berne, A.: Microphysics of Snowfall Over Coastal East Antarctica
         Simulated by Polar WRF and Observed by Radar, Journal of Geophysical Research: Atmospheres, 124, 11 452–11 476,
         https://doi.org/https://doi.org/10.1029/2019JD031028, 2019.

Table 1. Chirp table of WProf during the measurement campaign.

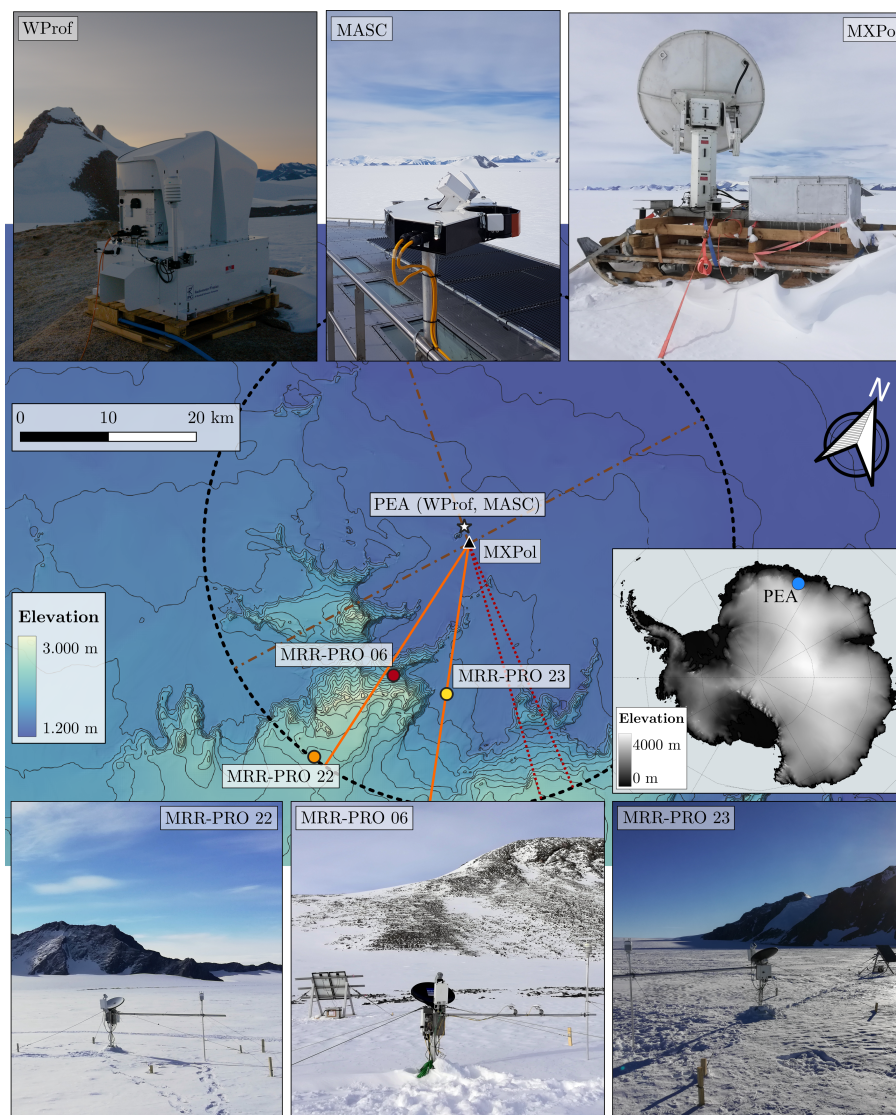| Chirp num.	Vertical range [m]	Vertical res. [m]	v_{ny} [m/s]	Vel. res. [m/s]
1	104 - 999	7.5	10.8	0.02
2	1008 - 3496	16.2	7.0	0.01
3	3512 - 8586	32.5	3.3	0.007

Figure 1. Elevation map of the region surrounding PEA. The markers and the accompanying text on the map highlights the location of the instruments deployed during the campaign. A picture of each of them is provided in the six panels above and below the map. The black dashed circle shows the maximum visibility radius of MXPol, while the coloured radii illustrate the direction of the RHI scans: the brown dash-dotted lines show the scan belonging only to the first cycle, the red dashed ones belong only to the second cycle, and the continuous orange ones belong to both. The small panel in the right-hand side of the figure shows the position of PEA on the Antarctic continent. In both panels the elevation has been derived from the REMA digital elevation model (Howat et al., 2019).
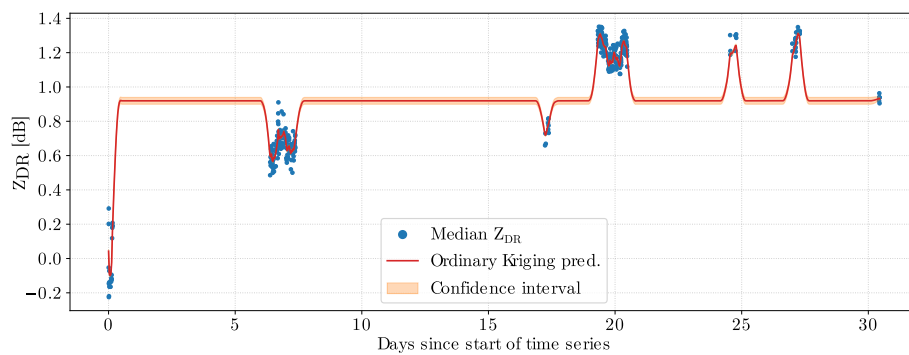
Figure 2. Time series of the differential reflectivity bias computed for MXPol. The continuous red line illustrates the final bias provided by the kriging interpolation, its uncertainty interval is highlighted in the orange, and the median offset derived from each vertical scan is displayed as blue dots.
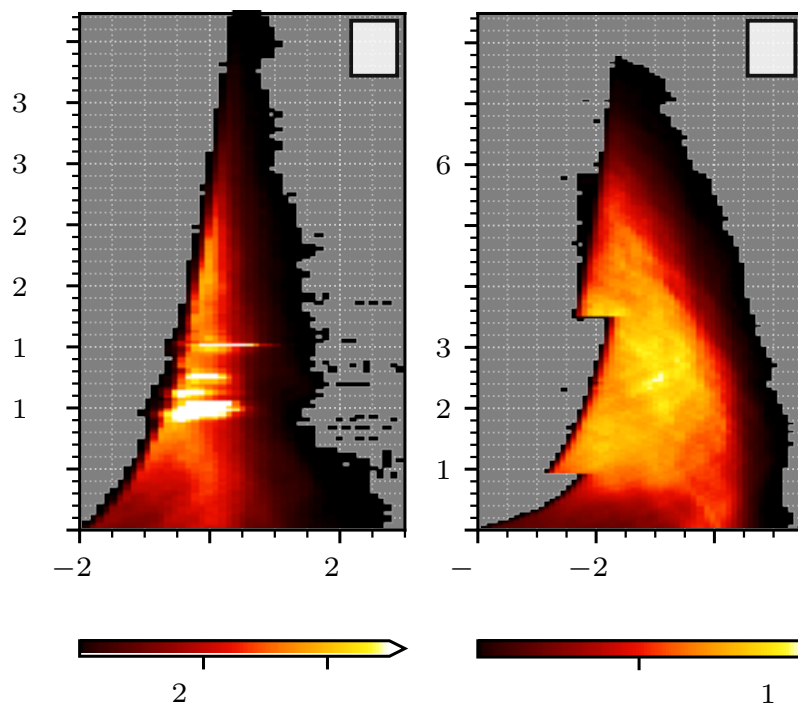
Figure 3. 2-dimensional distribution of the horizontal reflectivity factor collected by MXPol during the vertical scans (panel a) and the equivalent reflectivity factor recorded Wprof (panel b). A minimum threshold of 0 dB has been imposed on SNR for the two radars, with the additional condition $\rho_{hv} > 0.6$ for MXPol.
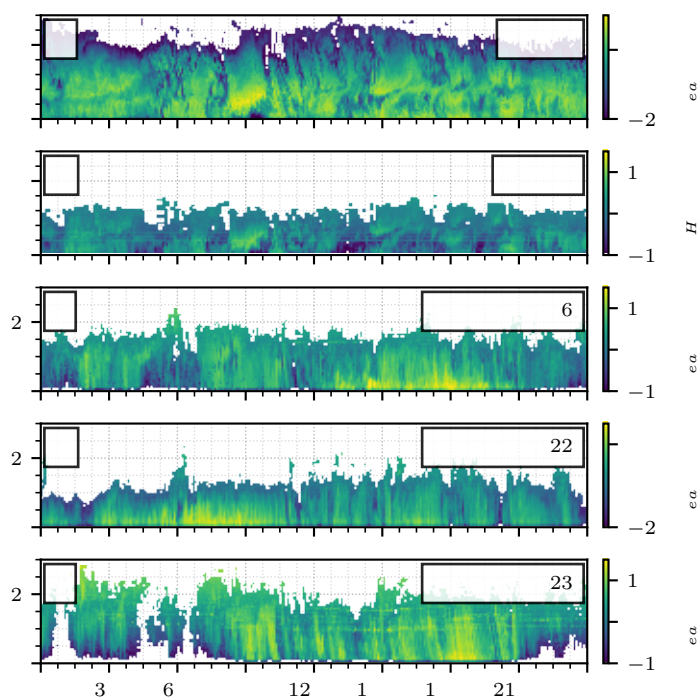
Figure 4. Measurements collected by the meteorological radars during the precipitation event on the 23 December 2019. The attenuated equivalent reflectivity factor collected by WProf and the three MRR-PRO is shown in panel a, c, d and e. Panel b shows the horizontal reflectivity factor recorded by MXPol during the vertical PPI scans. Conditions on SNR and ρ_{hv} analogous to the ones in Figure 3 have been enforced on all radars. Due to the limited sensitivity of the MRR-PRO, the vertical extent of the bottom three panels has been limited to the first 3 km of the profile.
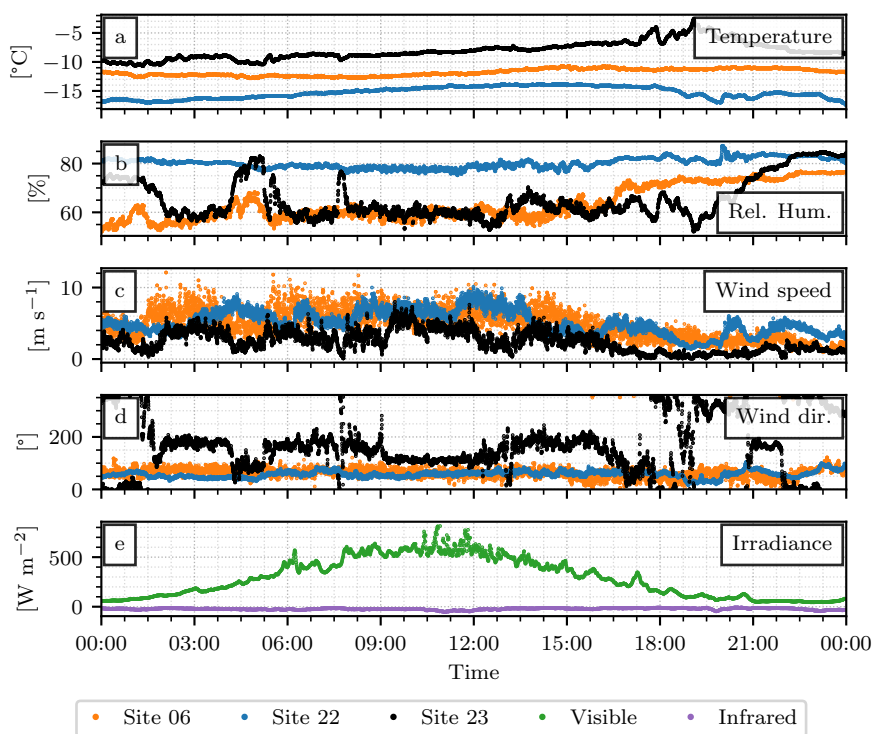
Figure 5. Measurements collected during the precipitation event on the 23 December 2019 by the automated weather stations and radiometers deployed alongside the three MRR-PRO. Four meteorological variables are displayed in the top four panels: temperature (panel a), relative humidity with respect to water (panel b), wind speed (panel c) and direction (panel d). The time-series at each panel is denoted by a different color: orange for the MRR-PRO 06 site, blue for the MRR-PRO 22 one, and black for the MRR-PRO 23 one. The downwelling irradiance in the shortwave (in green) and in the longwave (in purple) recorded by the radiometers co-located with the MRR-PRO 06 are shown in panel e.
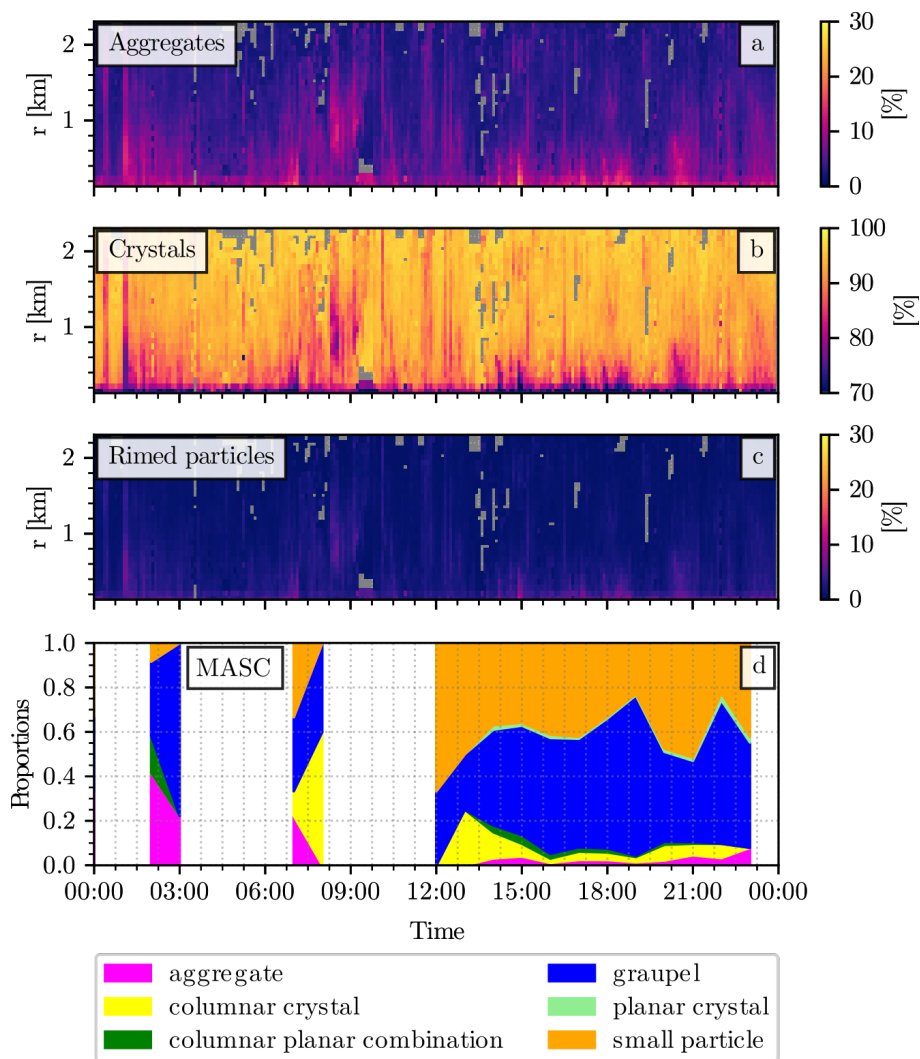
Figure 6. Information of the hydrometeor types derived from radar data and MASC images during the precipitation event on the 23 December 2019. The first three panels show the proportion of three hydrometeor classes computed using the algorithm described by Besic et al. (2018) from the RHI scans of MXPol performed above the base: snowflake aggregates in panel a, ice crystals in panel b and rimed particles in panel c. The hydrometeor types identified in the MASC images, using the method of Praz et al. (2017), are presented in panel d.
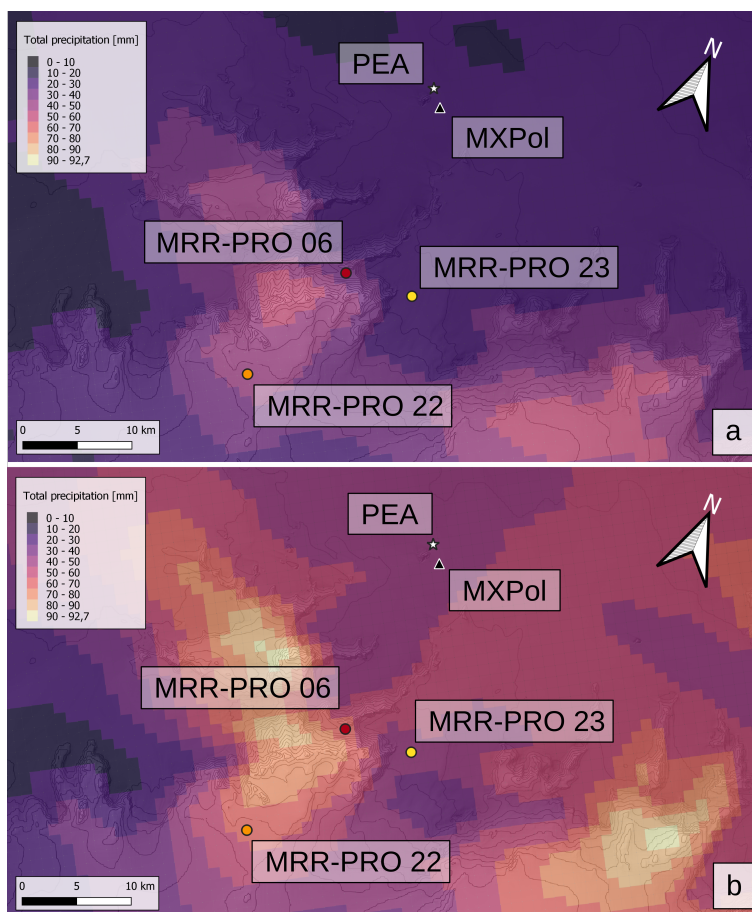
Figure A1. The total precipitation accumulation simulated by the WRF models in the innermost domain for December 2019 (panel a) and January 2020 (panel b), superimposed to a grayscale version of the digital elevation model already presented in Figure 1.